

Thermal Finite Element Modelling of the Laser Beam Welding of Tailor Welded Blanks through an Equivalent Volumetric Heat Source

Vito Busto

Universita degli Studi della Basilicata

Donato Coviello

Universita degli Studi della Basilicata

Andrea Lombardi

Universita degli Studi della Basilicata

Mariarosaria De Vito

Baosteel Tailored Blanks srl, Tito Scalo (PZ), Italy

Donato Sorgente (✉ donato.sorgente@unibas.it)

Universita degli Studi della Basilicata

Research Article

Keywords: laser beam welding, finite element modeling, volumetric heat source

Posted Date: July 9th, 2021

DOI: <https://doi.org/10.21203/rs.3.rs-667539/v1>

License:  This work is licensed under a Creative Commons Attribution 4.0 International License.

[Read Full License](#)

Thermal finite element modelling of the laser beam welding of tailor welded blanks through an equivalent volumetric heat source

Vito Busto¹, Donato Coviello¹, Andrea Lombardi¹, Mariarosaria De Vito², Donato Sorgente^{1*}

¹ School of Engineering, Università degli Studi della Basilicata, Via Ateneo Lucano, 10, 85100, Potenza, Italy

² Baosteel Tailored Blanks srl, Tito Scalo (PZ), Italy

* Corresponding author, donato.sorgente@unibas.it

Abstract

In last decades, several numerical models of the keyhole laser welding process were developed in order to simulate the joining process. Most of them are sophisticated multiphase numerical models tempting to include all the several different physical phenomena involved. However, less computationally expensive thermo-mechanical models that are capable of satisfactorily simulating the process were developed as well. Among them, a moving volumetric equivalent heat source, whose dimensions are calibrated on experimental melt pool geometries, can estimate some aspects of the process using a Finite Element Method (FEM) modelling with no need to consider fluid flows. In this work, a double-conical volumetric heat source is used to arrange a combination of two half hourglass-like shapes with different dimensions each other. This particular arrangement aims to properly assess the laser joining of a Tailor Welded Blank (TWB) even in case of butt joint between sheets of different thicknesses. Experiments of TWBs made of 22MnB5 steel sheets were conducted in both equal and different thicknesses configurations in order to validate the proposed model. The results show that the model can estimate in a satisfactory way the shape and dimensions of the fused zone in case of TWB made of sheets with different thickness.

Keywords: laser beam welding, finite element modeling, volumetric heat source

1. Introduction

In the framework of increasingly stricter pollutant emission regulations and the need of energy efficiency, Lutsey [1] pointed out as the automotive industry leads the technology development aimed to reduce energy consumption of vehicles. Graf [2] highlighted how such reduction can be achieved, for instance, by designing lighter cars through the use of materials with improved strength-to-weight ratios like aluminum alloys in substitution of steel. Hakamada et al. [3]

concluded that, although the use of parts made by magnesium and aluminium alloys requires more energy than steel at the production stage, the vehicle mass reduction increases fuel efficiency sufficiently to reduce the overall energy use. Mayyas et al. [4] claimed that another viable solution is redesigning and optimizing vehicle components/assemblies, or, where steel is needed for strength reasons, “tailoring” the whole structure such that specific material properties are located exactly where they are needed. As described by Merklein et al. [5], sheets with different chemical compositions, thicknesses or coating can be joined together to form, as it is called, a tailor-welded blank (TWB), a semi-finished product subjected, after joining, to a stamping process and designed to satisfy specified performances in specified locations. This technique allows the use of thicker or stronger materials in the critical regions of a component to reach structural and safety requirements, while thinner or lighter materials can be used in other regions to reduce the weight. Zadpoor et al. [6] reported that TWBs are commonly welded by laser welding from different sheets in the butt joint configuration prior to forming. The laser welding process is used for its well-known advantages such as high strength of the joint, deep penetration, localized heat affected zone, small distortions and high processing speed which results in high productivity. Hong and Shin [7] explained that the reasons why laser welding is a more attractive joining method compared to older ones are to be found in the abovementioned benefits. A coherent laser beam is focused on the surface of the piece to a small spot producing high power densities that quickly melt and partially vaporize the metal, generating a characteristic cavity known as “keyhole”, prevented from collapsing by the vapor pressure. Yan and Takayama [8] showed accurately how the laser-material interaction is a very complex phenomenon involving phase transformations and changes in chemical composition. However, the development of numerical models that are able to predict the weld pool geometry, thermal cycles or the effects of the welding, such as mechanical distortions, is useful to set and optimize process parameters. For these purposes, and other engineering problems, the complexity of the laser welding phenomena can be reduced by using an equivalent moving heat source calibrated with the experimental melt pool geometries, removing the fluid flow modelling difficulties without losing the capability to compute relevant data and to investigate some aspects of the process. There are several methods to simulate the heat input of the laser beam. Casalino et al. [9] modelled the moving source by associating an internal heat generation to specific elements in the weld zone, but, as reported by Aghaee Attar et al. [10] the most widespread methods are based on a moving volumetric heat source.

Several volumetric heat sources have been proposed in the last decades. Goldak et al. [11] proposed a non-axisymmetric three dimensional heat source in a double ellipsoid configuration. Although this model has been extensively used in FEM simulations, it is not applicable to deep penetration high density welding processes, such as keyhole processes. Du et al. [12] developed a heat source comprising a plane heat source on the top surface of the blank and a cylindrical heat source along laser beam axis, which takes into account the plasma effect and the keyhole absorption. Wu et al. [13] proposed a three-dimensional conical heat source, where the diameter of the heat intensity distribution region, characterized by a Gaussian form at any plane perpendicular to the laser beam axis, is linearly decreased along the thickness of the workpiece. However, neither the cylindrical shape nor the conical one are able to predict the root widening phenomenon of the weld pool associated with a deep penetration laser beam welding. Thus, new types of welding heat source were proposed. Farrokhi et al. [14] presented a modified version of the three dimensional conical heat source developed by Wu and coworkers, consisting in two conical moving heat sources, in which the heat density distribution region is first linearly decreased along the thickness and then it follows a reverse cone configuration to obtain an hourglass shape distribution. The same approach has been used by Zhan et al. [15]. To better calibrate the weld pool dimensions, a variable peak value of thermal flow along the thickness was used by Rong et al. [16]. In particular, the peak flux in the center of each plane perpendicular to the laser beam axis was expressed as a function of the distance from the middle plane and of an adjustment coefficient. Depending on the value of this coefficient, the peak flux is increased or decreased along the thickness direction. Because of the axial symmetry of the volumetric heat sources presented so far, welding between blanks of same thickness can only be modelled. However, TWBs are often characterized by welding of blanks with different thicknesses, in which the fused zone shape is asymmetric and it can be represented as a combination of two half hourglass-like shapes, each with specific dimensions depending on thickness. Koo et al. [17] studied the phenomena involved during laser welding that promote the formation of a hourglass shaped fusion zone in TWB. However, their numerical results are presented in an iso-thickness configuration. Li et al. [18] investigated by experiments and numerical simulations the effect of process parameters on the shape of the welding pool during laser welding of dissimilar thicknesses. In their study, they demonstrated that the difference in thickness in the butt joint has a large impact on the weld deviation since it creates different cooling rates. In spite of this, in their experiments the depth of

the fusion zone was identical in the two welded thicknesses. This is not the case in a common industrial TWB.

The aim of this work is to develop a new volumetric heat source to be implemented in a FEM simulation based on thermal conduction heat transfer and capable to predict the dimensions of a double half hourglass weld pool shape of a full penetration laser welding performed on TWB composed from sheets with different thicknesses. The parameters of a variable peak flux heat source with a double conical shape were found by the energy balance differentiating them from the two different thicknesses. The heat source was calibrated first using two iso-thickness welding configurations and then on a different thickness welding configuration.

2. Material and methods

2.1 Experimental procedure

Laser welding experiments have been conducted by Baosteel Tailored Blanks Italy on Al-Si coated 22MnB5 steel sheets. The sheets thicknesses were 1.2 and 1.5 mm, whereas the coating thickness was nominally 30 μm . Steel sheets were laser-welded by a TRUMPF TruDisk 6006 solid-state disk laser (specifications listed in Table 1) and a weld system for linear and non-linear welding.

Table 1: Specifications of laser welding system.

Laser welding source	TRUMPF TruDisk 6006 solid-state disk laser
Laser wavelength (nm)	1030
Beam Parameter Product, BPP (mm·mrad)	25
Focusing length (mm)	200
Focal diameter (mm)	0.6
Diameter of collimated beam (mm)	33
Rayleigh length (mm)	3.6

Experiments were run in three different configurations. Sheets of the same thickness were joined in two configurations (1.2-1.2 mm and 1.5-1.5 mm), whereas the third one concerned the welding of different thicknesses (1.5-1.2 mm). The same process parameters were adopted for all the configurations described. The welding speed was 5 m/min, the laser power was 5.4 kW. The focal plane was positioned at 1.5 mm over the clamping table, and the beam axis was positioned at 0.08 mm from the weld line (in the different thicknesses configuration, the beam axis always hit the

thicker sheet). The shielding gas was Argon, blown on the upper surface of the sheets (the nozzle was inside the laser head), with a flow rate of 17 l/min. For any configuration, the steel sheets were welded in the as-received condition without any filler material, so the Al-Si layer was not removed. After welding, the specimens were prepared for the metallographic analysis in the as-welded condition. No heat treatment was performed on the welded joints in order to preserve a good visual differentiation of fused zone. The cross sections of the welded joints were cut with the precision cutting machine Struers Secotom-50, mounted with the mounting press Struers CitoPress-30, and then ground and polished with the automatic polisher Struers Tegramin-25. Finally, specimens were etched with a 2% Nital solution and observed by optical microscopy.

2.2 Heat source model

In order to accurately describe the weld geometry between two sheets of different thickness, the peak index increment-double cone (PII-DC) heat source, proposed by Rong et al. [16], has been appropriately modified. As shown in Fig. 1, the heat source used is composed of two double conical sources, one for each sheet, combined with two further three-dimensional elements called "conical hoofs" capable of reproducing the bevel generated by welding of sheets of different thickness. Each "conical hoof" represents one of the two parts obtained by cutting, with an inclined plane, a half truncated cone.

Assuming that the heat flow q_l , in each cross section, is characterized by a Gaussian distribution and that its peak value q_m varies along the thickness direction (z-direction), the heat source can be mathematically expressed using the following formulation

$$q_l(r, z) = q_m(z) \cdot \exp\left(-\frac{3r^2}{r_0^2}\right) \quad (1)$$

where r_0 is the distribution parameter (linearly variable along the thickness) and r is the radial coordinate. For a moving laser heat source in y direction with a welding speed v , we have

$$r = \sqrt{(y - vt)^2 + x^2} \quad (2)$$

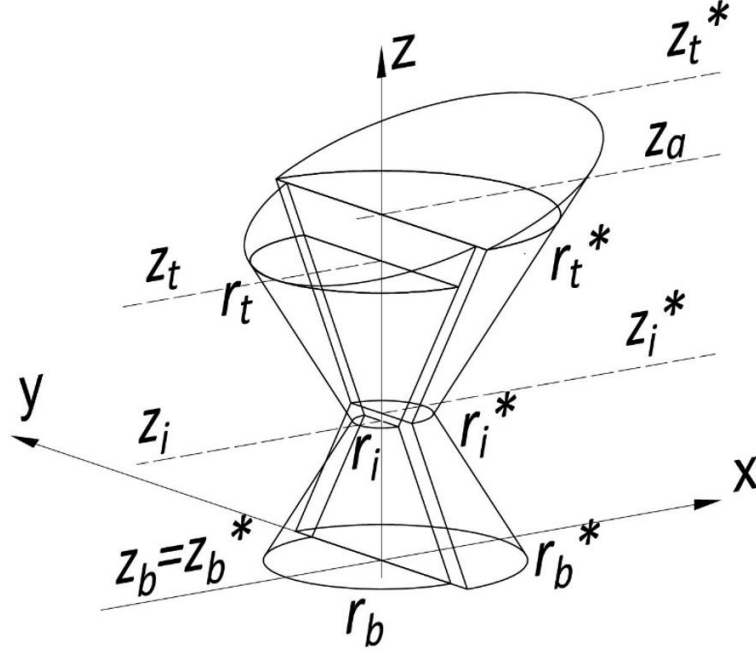


Fig. 1. Schematic diagram of the proposed heat source model.

With reference to Fig. 2a, for each zone of the heat source, the distribution parameter r_0 can be expressed as

$$r_{01}(z) = r_i - (r_i - r_b) \frac{z_i - z}{z_i - z_b} \quad z_b \leq z < z_i \quad (3)$$

$$r_{02}(z) = r_t - (r_t - r_i) \frac{z_t - z}{z_t - z_i} \quad z_i \leq z \leq z_a \quad (4)$$

$$r_{01}^*(z) = r_i^* - (r_i^* - r_b^*) \frac{z_i^* - z}{z_i^* - z_b^*} \quad z_b^* \leq z < z_i^* \quad (5)$$

$$r_{02}^*(z) = r_t^* - (r_t^* - r_i^*) \frac{z_t^* - z}{z_t^* - z_i^*} \quad z_i^* \leq z \leq z_t^* \quad (6)$$

where $r_b, r_i, r_t, z_b, z_i, z_t, z_a, r_b^*, r_i^*, r_t^*, z_b^*, z_i^*$ and z_t^* are 13 defined parameters to describe the shape of the laser weld; the star apex indicates the quantities relating to the thicker sheet while the subscripts 1 and 2 indicate, respectively, the lower and upper zone of the heat source.

The value of the thermal flux at the center of the heat source $q_m(z)$ is expressed as a function of a peak index λ using the following equations.

$$q_{m1}(z) = q_0 \exp\left(\ln \lambda_1 \frac{z_i - z}{z_i - z_b}\right) \quad z_b \leq z < z_i \quad (7)$$

$$q_{m2}(z) = q_0 \exp\left(\ln \lambda_2 \frac{z - z_i}{z_a - z_i}\right) \quad z_i \leq z \leq z_a \quad (8)$$

$$q_{m1}^*(z) = q_0 \exp\left(\ln \lambda_1^* \frac{z_i^* - z}{z_i^* - z_b^*}\right) \quad z_b^* \leq z < z_i^* \quad (9)$$

$$q_{m2}^*(z) = q_0 \exp\left(\ln \lambda_2^* \frac{z - z_i^*}{z_t^* - z_i^*}\right) \quad z_i^* \leq z \leq z_t^* \quad (10)$$

where q_0 is the peak value at the z_i and z_i^* sections

$$q_m(z_i) = q_m^*(z_i^*) = q_0 \quad (11)$$

Substituting Eq. (7), (8), (9) and (10) into Eq. (1), the heat flow can be written as

$$q_{l1}(r, z) = q_0 \exp\left(\ln \lambda_1 \frac{z_i - z}{z_i - z_b}\right) \exp\left(-\frac{3r^2}{r_{01}^2}\right) \quad z_b \leq z < z_i \quad (12)$$

$$q_{l2}(r, z) = q_0 \exp\left(\ln \lambda_2 \frac{z - z_i}{z_a - z_i}\right) \exp\left(-\frac{3r^2}{r_{02}^2}\right) \quad z_i \leq z \leq z_a \quad (13)$$

$$q_{l1}^*(r, z) = q_0 \exp\left(\ln \lambda_1^* \frac{z_i^* - z}{z_i^* - z_b^*}\right) \exp\left(-\frac{3r^2}{r_{01}^{*2}}\right) \quad z_b^* \leq z < z_i^* \quad (14)$$

$$q_{l2}^*(r, z) = q_0 \exp\left(\ln \lambda_2^* \frac{z - z_i^*}{z_t^* - z_i^*}\right) \exp\left(-\frac{3r^2}{r_{02}^{*2}}\right) \quad z_i^* \leq z \leq z_t^* \quad (15)$$

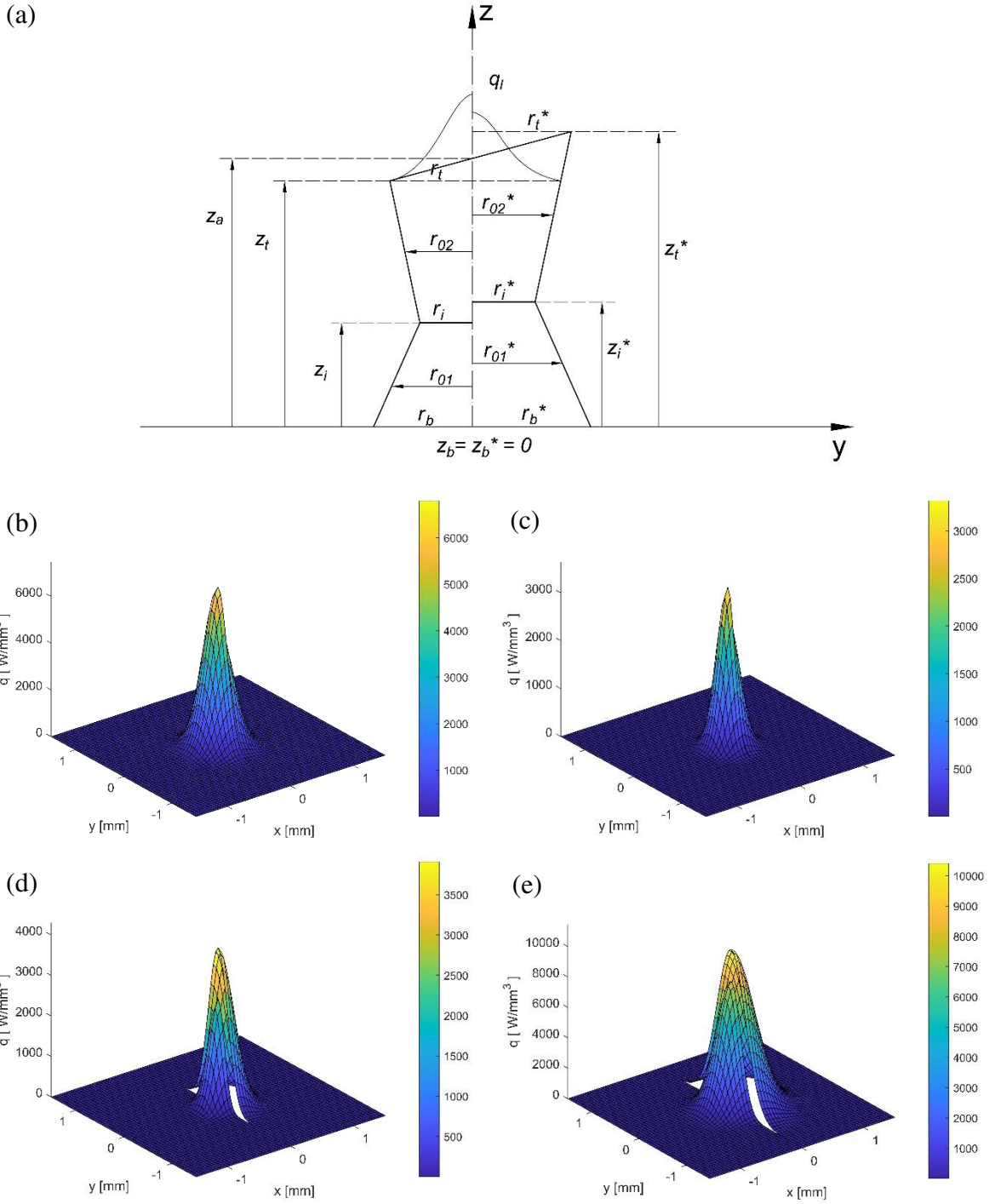


Fig. 2. (a) 2D schematic of the heat source and heat intensity distribution at (b) z_t plane, (c) z_t^* plane, (d) z_i plane and (e) the bottom surface.

Heat source parameters: $P = 5,4 \text{ kW}$, $\eta_l = 0,28044$, $\alpha = 2$, $z_i = 1,2 \text{ mm}$, $r_t = 0,471 \text{ mm}$, $z_t = 1,2 \text{ mm}$, $r_i = 0,471 \text{ mm}$, $z_r = 1,2 \text{ mm}$, $r_t = 0,471 \text{ mm}$, $z_a = 1,324 \text{ mm}$, $r_t = 0,471 \text{ mm}$, $z_t = 1,2 \text{ mm}$, $r_i = 0,314 \text{ mm}$, $z_i = 0,45 \text{ mm}$, $r_b = 0,494 \text{ mm}$, $r_t^* = 0,517 \text{ mm}$, $z_t^* = 1,5 \text{ mm}$, $r_i^* = 0,378 \text{ mm}$, $z_i^* = 0,629 \text{ mm}$, $r_b^* = 0,743 \text{ mm}$.

The adjustment coefficients ($\lambda_1, \lambda_2, \lambda_1^*$ and λ_2^*) for the upper and lower zones of the heat source, respectively for thin and thick sheet, are expressed using the following equations.

$$\lambda_1 = \alpha \cdot \frac{r_b}{r_i} \quad (16)$$

$$\lambda_2 = \alpha \cdot \frac{r_t}{r_i} \quad (17)$$

$$\lambda_1^* = \alpha \cdot \frac{r_b^*}{r_i^*} \quad (18)$$

$$\lambda_2^* = \alpha \cdot \frac{r_t^*}{r_i^*} \quad (19)$$

where α is a coefficient introduced to synchronously regulate $\lambda_1, \lambda_2, \lambda_1^*$ and λ_2^* .

The key problem is how to determine the parameter q_0 . According to thermal energy conservation law, indicating with P_l the laser power and with η_l the energy transfer efficiency (ETE) of laser, an equilibrium equation was developed

$$\eta_l P_l = Q_l = \sum_k Q_{lk} = \sum_k \left(\iiint_{V_k} q_l(r, z) r dr d\theta dz \right) \quad k = 1, 2, 3, 1^*, 2^*, 3^* \quad (20)$$

Into Eq. (20), Q_l represents the effective laser power and is distributed within the heat source in different quotas Q_{lk} , proportional to the volume V_k of each part that composes it.

For truncated cone parts, Q_{lk} can be expressed as

$$Q_{l1} = \int_{z_b}^{z_i} \int_0^\pi \int_0^{r_{01}} q_{l1}(r, z) r dr d\theta dz \quad (21)$$

$$Q_{l2} = \int_{z_i}^{z_t} \int_0^\pi \int_0^{r_{02}} q_{l2}(r, z) r dr d\theta dz \quad (22)$$

$$Q_{l1^*} = \int_{z_b^*}^{z_i^*} \int_0^\pi \int_0^{r_{01}^*} q_{l1}^*(r, z) r dr d\theta dz \quad (23)$$

$$Q_{l2^*} = \int_{z_i^*}^{z_a} \int_0^\pi \int_0^{r_{02}^*} q_{l2}^*(r, z) r dr d\theta dz \quad (24)$$

Due to the symmetry of the heat source with respect to the x - z plane, Q_{I3} and Q_{I3^*} , quantities referring to the “conical hoofs” (see Appendix 1), can be written as

$$Q_{I3} = 2 \cdot \int_{z_t}^{z_a} \left(\int_0^\varphi \int_0^{r_3} q_{I2}(r, z) r dr d\theta + \int_\varphi^{\pi/2} \int_0^{r_{02}} q_{I2}(r, z) r dr d\theta \right) dz \quad (25)$$

$$Q_{I3^*} = 2 \cdot \int_{z_a}^{z_t^*} \int_0^{\varphi^*} \int_{r_3^*}^{r_{02}^*} q_{I2}^*(r, z) r dr d\theta dz \quad (26)$$

As shown in Eq. (27), isolating the initial peak value of thermal flow q_0 from Eq. (21), (22), (23), (24), (25) and (26), it can be expressed as

$$q_0 = \frac{\eta_l P_l}{I_1 + I_2 + I_3 + I_1^* + I_2^* + I_3^*} \quad (27)$$

where $I_1, I_2, I_3, I_1^*, I_2^*$ and I_3^* are the values of the integrals made clear in the Appendix 2.

2.3 Finite element modelling

After the definition of the heat source model, the weld pool geometry and the temperature profile were determined by FEM. For the simulations, the commercially available software ABAQUS\CAE was used.

In absence of data of some of the thermo-physical properties of the material, such as latent heat of fusion and vaporization, liquidus and solidus temperature, the values referred to chemically similar steels and to pure iron were picked from Wang et al. [19], while density, specific heat capacity and thermal conductivity were extracted from the work of Kaars et al. [20]. Thermo-physical properties of the investigated steel are summarized in Table 2.

Three case studies were considered. The first two cases employed two sheets of thicknesses 1.2 mm and 1.5 mm, respectively, to determine the energy transfer efficiency, which can be very low for thin plates, as demonstrated by Swift-Hook and Gick [21] and dependent on the thickness of the sheet as can be seen in the work of Sharma and Molian [22]. Secondly, an average value of the ETE was imposed for the simulation of the TWB obtained from the welding of the sheets with the above mentioned initial thicknesses of 1.2 and 1.5 mm. To save computational time in the first two cases, the full size of the specimen was reduced to a symmetric sheet of size 12.5 mm x 25 mm. The model is shown in Fig. 3. For the same reason, this portion of the sheet was divided into three

regions with different mesh refinement, as can be seen in Fig. 4, with the finer one constructed by structured hex elements of type DC3D8, an 8-node linear heat transfer brick of dimensions 0.1 mm x 0.1 mm.

Table 2. Thermo-physical properties of the material implemented in the numerical simulation

Property	Magnitude
Density, ρ	7807 kg/m ³
Solidus temperature, T_s	1693 K
Liquidus temperature, T_L	1733 K
Latent heat of fusion, L_f	250 KJ/kg
Latent heat of vaporization, L_v	6.289 MJ/kg
Boiling temperature, T_v	3273 K
Specific heat capacity, c	$c(T)$
Thermal conductivity, k	$k(T)$

On the top surface of the sheet and on the bottom surface of the welding bead region, a constant convection heat transfer coefficient of $h=10 \text{ W/m}^2\text{K}$ was imposed, together with an emissivity of 0.5 applied to the whole part. The effect of the shielding gas was neglected since an insignificant influence in temperature distribution of a much higher value of h was found. A transient heat transfer procedure was set, with no mechanical boundary conditions and a welding time period of 0.2 seconds. The new volumetric heat source was implemented by an external subroutine called DFLUX, available in the ABAQUS library, defining a non-uniform distributed flux as a function of position and time. The same assumptions, except for the symmetry, have been made for the TWB. In this case, the geometry of the weld bead was constructed from the acquired macrographs, taking into account the peculiar bevel feature.

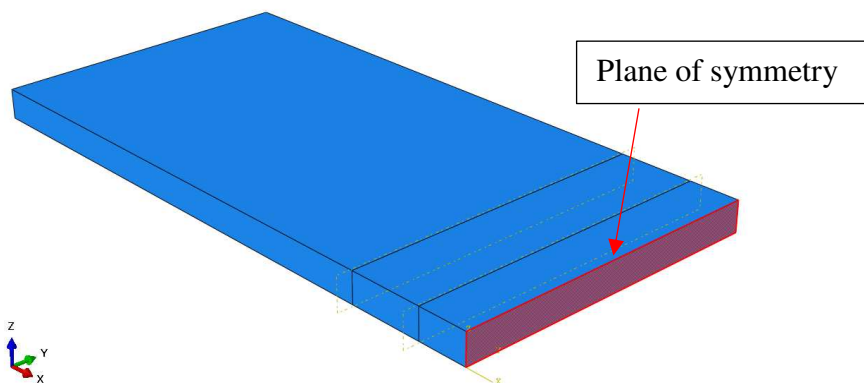


Fig. 3. Symmetric plate of size 12.5 mm x 20 mm.

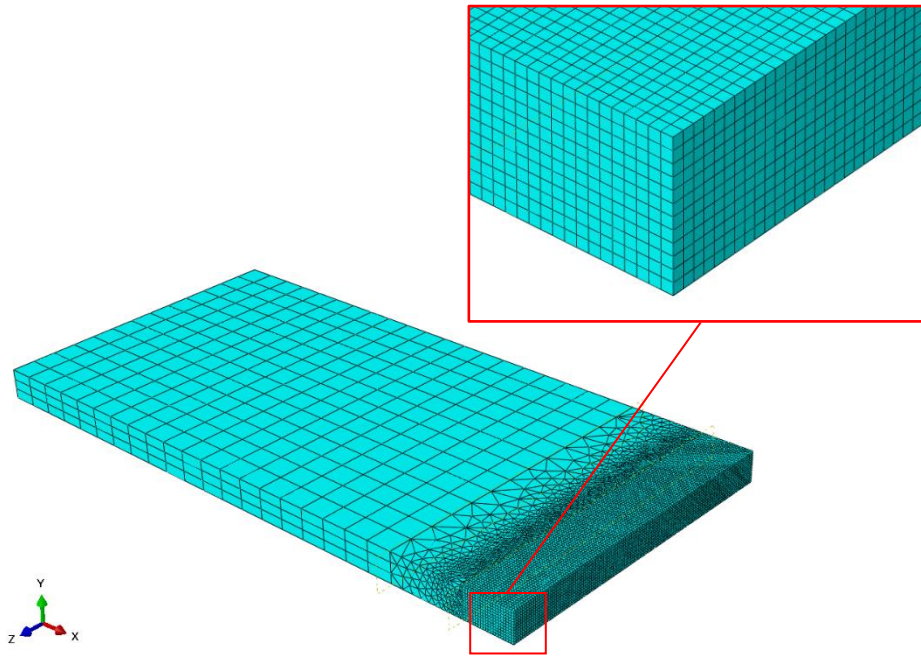


Fig. 4. Finite element mesh with three level of mesh refinement and detail view of the finest one.

3. Results and discussion

3.1 Welding results

Fig. 5 shows the cross sections of welded joints in the as-welded conditions. A full-penetrated weld with an hourglass shape was achieved in all the considered combinations, so the aforementioned double conical heat source model was considered suitable for all the configurations. In Table 3, the cross sections measurements according to the geometrical parameters of the double conical heat source model defined in Figure 2a, are reported.

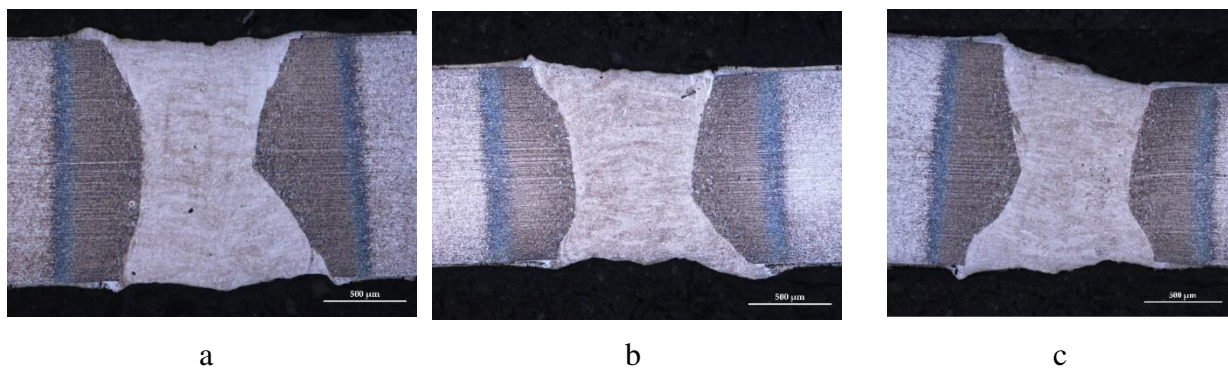


Fig. 5. Cross sections of welded joints in as-welded conditions and related geometrical dimensions according to double conical heat source model: (a) 1.5-1.5 mm; (b) 1.2-1.2 mm; (c) 1.5-1.2 mm.

Table 3. Geometrical parameters of the welding experiments in the three different configurations

Dimension	1.5 mm – 1.5 mm	1.2 mm – 1.2 mm	1.5 mm – 1.2 mm
rb, mm	0.636	0.585	0.494
ri, mm	0.340	0.351	0.314
rt, mm	0.565	0.554	0.471
zi, mm	0.719	0.448	0.450
rb*, mm	-	-	0.743
ri*, mm	-	-	0.378
rt*, mm	-	-	0.517
zi*, mm	-	-	0.629

3.2 Numerical results

The first step was to calibrate the model in the iso-thickness configurations (1.2 mm and 1.5 mm) through the corresponding experimental profile. In order to reduce the number of calibration parameters, the double conical heat source model developed by Farrokhi et al. [14], with the effective laser power distributed in the lower and upper cone, as shown in the work by Thasanaraphan [23], was applied. In that formulation, the only unknown (and uncertain) parameter affecting the dimension of the weld bead was the ETE. Thus, a variable ETE in the range between 0.1 and 0.9 was implemented in the simulations. The experimental and the simulated values of the area of the fused zone in the cross-section of the weld bead were compared and the difference between the two was minimized by linear interpolation as shown in Fig. 6. The values of the ETE in the two cases were found to be very low compared to values that can be as high as 90% or more for key-hole processes, as pointed out by Swift-Hook and Gick [21]. However these results are consistent with those found by Sharma and Molian [22] and by Swift-Hook and Gick [21] for thin plates. In welding thin sheets with large power level like in the investigated cases, a through thickness keyhole is usually formed, letting a large portion of the laser light to be transmitted beyond the sheets. For the thinner sheet (1.2 mm) a value of 0.244 was found, while for the thicker one (1.5 mm) a value of 0.317 minimized the above mentioned difference. Results with the corresponding ETE values are depicted in Fig. 7. An average ETE value of 0.2805 between these two was used for the TWBs subsequent simulations.

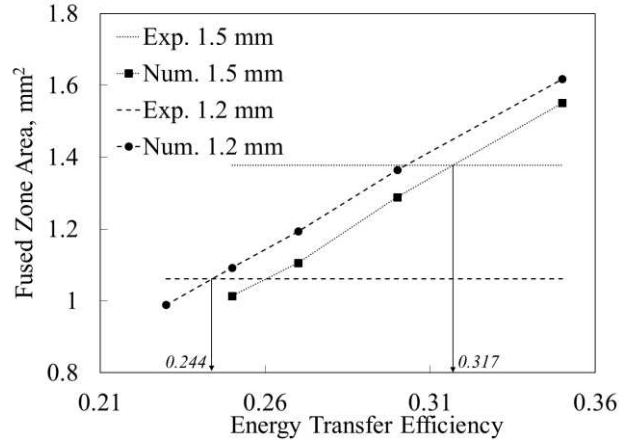


Fig. 6. Numerical results with different values of the energy transfer efficiency for the iso-thickness configurations.

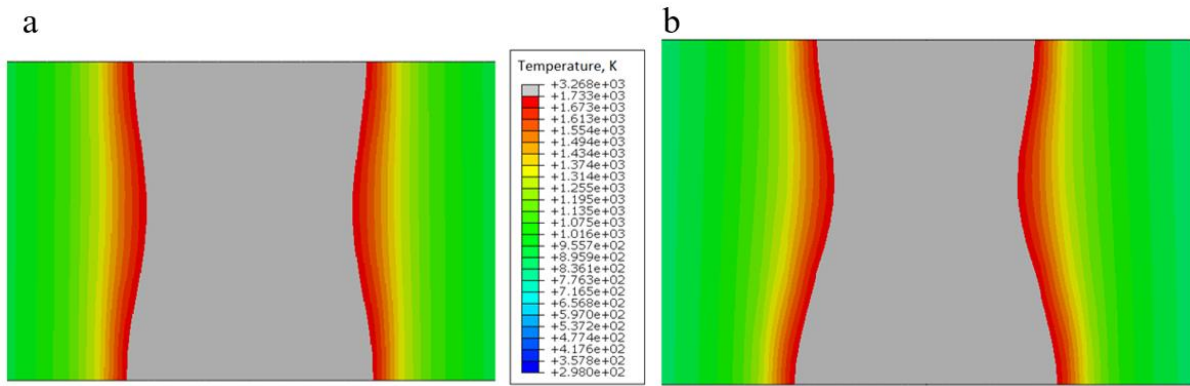


Fig. 7. Cross-section of the melt pool geometries of the two sheets: a) 1.2 mm, b) 1.5 mm. The grey area represents the fused zone.

To calibrate the fused zone in the TWB a variable α (1, 2, 4, 6) was imposed, with fixed ETE and fixed geometrical dimensions (r_b , r_t , r_i , r_b^* , r_t^* , r_i^*). Results, in terms of geometrical parameters, are shown in Table 4 together with the value of q_0 calculated solving Eq. 27 for different α values. A value of $\alpha=6$ was found to minimize the error between experimental and simulation values. Numerical results for $\alpha=6$, including the body heat flux, are shown in Fig. 8.

As it can be seen by Table 4 and Fig. 8, while an acceptable average error was achieved, especially on characteristics radii dimensions, a significant deviation persist in the prediction of the neck height both in the best alpha configuration and the other simulated ones. No such large errors were found neither by Farrokhi et al. [14] nor by Rong et al. [16] in the iso-thickness configuration. Thus, one possible reason of this deviations could be the different heat diffusion phenomena along the sheets that takes place in welds with different thicknesses.

Table 4. Deviations between experimental and numerical values of the fused zone dimensions.

Dimension	$\alpha=1$ $q_0 = 4.060 \times 10^{12}$ W/m ³		$\alpha=2$ $q_0 = 2.647 \times 10^{12}$ W/m ³		$\alpha=4$ $q_0 = 1.673 \times 10^{12}$ W/m ³		$\alpha=6$ $q_0 = 1.263 \times 10^{12}$ W/m ³	
	Value, mm	Deviation, mm	Value, mm	Deviation, mm	Value, mm	Deviation, mm	Value, mm	Deviation, mm
	r_b	0.49	0.004	0.51	-0.016	0.52	-0.026	0.52
r_i	0.37	-0.056	0.35	-0.036	0.33	-0.016	0.31	0.004
r_t	0.44	0.031	0.44	0.031	0.46	0.011	0.46	0.011
z_i	0.89	-0.44	0.89	-0.44	0.86	-0.41	0.86	-0.41
r_b^*	0.75	-0.007	0.77	-0.027	0.8	-0.057	0.82	-0.077
r_i^*	0.44	-0.062	0.41	-0.032	0.4	-0.022	0.39	-0.012
r_t^*	0.41	0.107	0.43	0.087	0.45	0.067	0.45	0.067
z_t^*	1.11	-0.481	1.13	-0.501	1.09	-0.461	1.05	-0.421

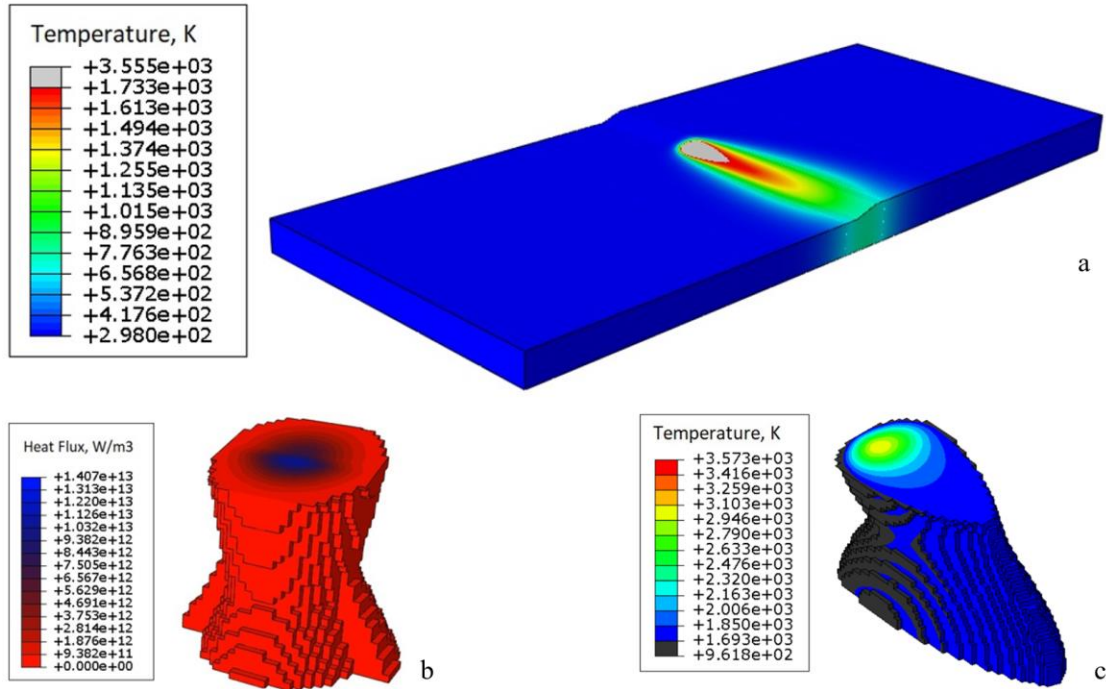


Fig. 8. Numerical results on the different thickness configuration with $\alpha=6$. (a) Temperature distribution on the TWB; (b) Volume in which the body heat flux is applied with related values; (c) volume of the material where the temperature is above the solidus.

While few experimental observations of the molten pool are available in previous studies like the one by Artinov et al. [24], several published numerical results indicates that the width of the molten pool is usually larger (transversal direction), as shown by Zhan et al. [15], and longer (longitudinal direction), as shown by Artinov et al. [25], on the weld top rather on the bottom, contrary to what was found in this work (Fig. 8c). It should be recalled that published works, dealing with both

experimental and numerical results, are related to iso-thickness configurations and heat diffusion in the joint is strongly influenced by the thickness of the welded sheet. It is thought that upper part of the weld pool is likely to be more rapidly cooled down by the greater heat losses in the upper part of the joint since the different thickness are welded with the lower edge at the same z level. A different weighting of the geometrical parameters or a different distribution of the heat flux along the thickness and/or between the two different thicknesses is beyond the scope of this work and could be considered as future investigations for improving the achieved results.

Conclusions

An original approach for applying a volumetric heat source to a laser beam welding configuration where a butt joint involve different thickness was developed and assessed. The energy balance was applied to find the parameters of the peak index increment-double cone heat source combined with two further three-dimensional elements called "conical hoofs" capable of reproducing the bevel generated by welding of sheets of different thickness with and hourglass shaped fusion zone. Two iso-thickness configurations were used to find a suitable energy transfer efficiency for the different thickness configurations. Numerical results in the dissimilar thickness configuration show a fairly good prediction capability of the model in terms of dimensions of the fused zone into the weld. Larger discrepancies were found in the prediction of the height of the hourglass neck.

Acknowledgments

The authors express their gratitude to the personnel of Baosteel Tailored Blanks Italy for the experimental support on this work and to Pasquale Guglielmi and Gianfranco Palumbo of Polytechnic University of Bari for their help in the metallographic analyses.

Declarations

Funding

Not applicable

Conflicts of interest

The authors declare no competing interests.

Availability of data and material

The authors confirm that the data supporting the findings of this study are available within the article.

Code availability

Not applicable

Ethics approval

Not applicable

Consent to participate

Not applicable

Consent for publication

Not applicable

Appendix 1

For the "conical hoof" of thin sheet the distribution parameter r_0 is not uniquely defined. In fact, as shown in Fig. A1.1, it coincides with r_{02} only for $\varphi \leq \theta \leq \pi/2$. For $0 \leq \theta \leq \varphi$ we can define a new variable parameter along the z-direction and variable with θ , $r_3(z, \theta)$. Indicating with $w(z)$ the projection of r_3 along the x-axis, we have

$$w(z) = r_3(z, \theta) \cdot \cos\theta \quad (\text{A1-1})$$

When $\theta = \varphi$, r_{02} and r_3 coincide. Using this property, we can write

$$w(z) = r_{02}(z) \cdot \cos\varphi \quad (\text{A1-2})$$

In addition, for properties of similar triangles, we have

$$w(z) = r_t \frac{z_a - z}{z_a - z_t} \quad (\text{A1-3})$$

By substituting Eq. A1-3, respectively, in Eq. A1-1 and in Eq. A1-2, the volumetric integration limits can be expressed as

$$\begin{cases} r_3(z, \theta) = \frac{r_t}{\cos\theta} \cdot \frac{z_a - z}{z_a - z_t} \\ \varphi(z) = \cos^{-1} \left(\frac{r_t}{r_{02}(z)} \cdot \frac{z_a - z}{z_a - z_t} \right) \end{cases} \quad z_t \leq z \leq z_a; -\varphi \leq \theta \leq \varphi \quad (\text{A1-4})$$

Similarly, with reference to Fig. A1.2, the volumetric integration limits for thick sheet can be expressed as

$$\begin{cases} r_3^*(z, \theta) = \frac{r_t^*}{\cos\theta} \cdot \frac{z - z_a}{z_t^* - z_a} \\ \varphi^*(z) = \cos^{-1} \left(\frac{r_t^*}{r_{02}^*(z)} \cdot \frac{z - z_a}{z_t^* - z_a} \right) \end{cases} \quad z_a \leq z \leq z_t^*; \quad -\varphi^* \leq \theta \leq \varphi^* \quad (\text{A1-5})$$

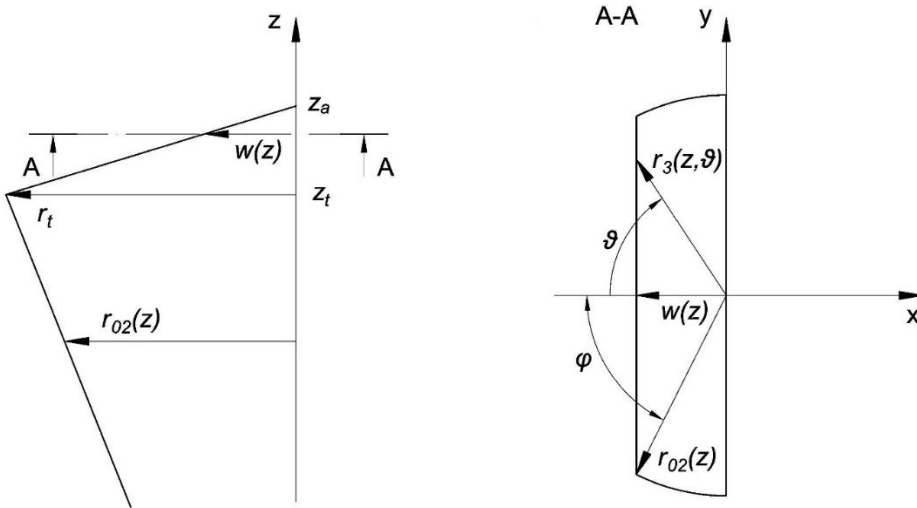


Fig. A1.1 Geometric parameters of the “conical hoof” for thin sheet.

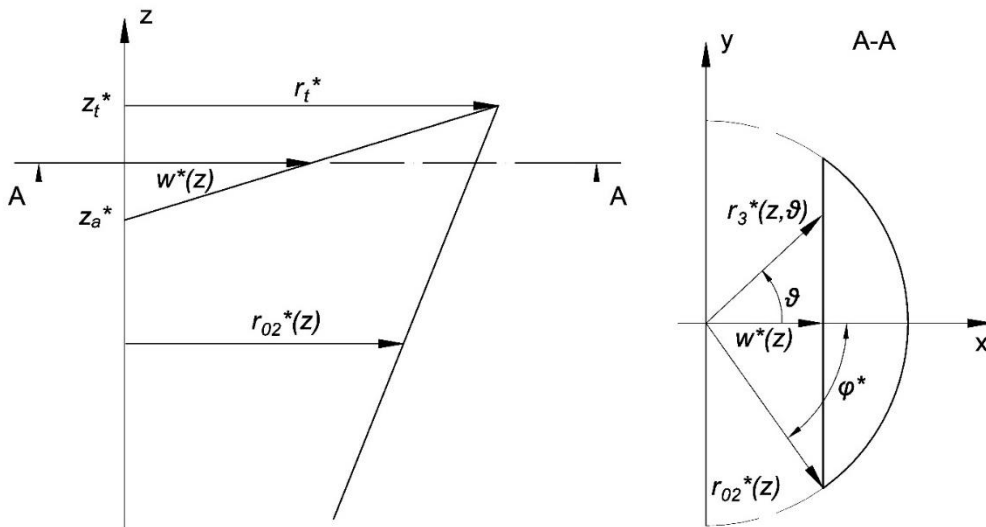


Fig. A1.2 Geometric parameters of the “conical hoof” for thick sheet.

Appendix 2

$$I_1 = \int_{z_b}^{z_i} \int_0^\pi \int_0^{r_{01}} \exp\left(\ln \lambda_1 \frac{z_i - z}{z_i - z_b}\right) \exp\left(-\frac{3r^2}{r_{01}^2}\right) r dr d\theta dz \quad (\text{A2-1})$$

$$I_2 = \int_{z_i}^{z_t} \int_0^\pi \int_0^{r_{02}} \exp\left(\ln \lambda_2 \frac{z - z_i}{z_a - z_i}\right) \exp\left(-\frac{3r^2}{r_{02}^2}\right) r dr d\theta dz \quad (\text{A2-2})$$

$$I_3 = 2 \cdot \int_{z_t}^{z_a} \left(\int_0^\varphi \int_0^{r_3} \exp\left(\ln \lambda_2 \frac{z - z_i}{z_a - z_i}\right) \exp\left(-\frac{3r^2}{r_{02}^2}\right) r dr d\theta \right. \\ \left. + \int_{\frac{\pi}{2}}^\pi \int_0^{r_{02}} \exp\left(\ln \lambda_2 \frac{z - z_i}{z_a - z_i}\right) \exp\left(-\frac{3r^2}{r_{02}^2}\right) r dr d\theta \right) dz \quad (\text{A2-3})$$

$$I_1^* = \int_{z_b^*}^{z_i^*} \int_0^\pi \int_0^{r_{01}^*} \exp\left(\ln \lambda_1^* \frac{z_i^* - z}{z_i^* - z_b^*}\right) \exp\left(-\frac{3r^2}{r_{01}^{*2}}\right) r dr d\theta dz \quad (\text{A2-4})$$

$$I_2^* = \int_{z_i^*}^{z_a} \int_0^\pi \int_0^{r_{02}^*} \exp\left(\ln \lambda_2^* \frac{z - z_i^*}{z_t^* - z_i^*}\right) \exp\left(-\frac{3r^2}{r_{02}^{*2}}\right) r dr d\theta dz \quad (\text{A2-5})$$

$$I_3^* = 2 \cdot \int_{z_a}^{z_t^*} \int_0^{\varphi^*} \int_{r_3^*}^{r_{02}^*} \exp\left(\ln \lambda_2^* \frac{z - z_i^*}{z_t^* - z_i^*}\right) \exp\left(-\frac{3r^2}{r_{02}^{*2}}\right) r dr d\theta dz \quad (\text{A2-6})$$

References

1. Lutsey N (2012) Regulatory and technology lead-time: The case of US automobile greenhouse gas emission standards. *Transp Policy* 21:179–190. <https://doi.org/10.1016/j.tranpol.2012.03.007>
2. Graf A (2021) Aluminum alloys for lightweight automotive structures. *Mater Des Manuf Light Veh* 97–123. <https://doi.org/10.1016/b978-0-12-818712-8.00003-3>
3. Hakamada M, Furuta T, Chino Y, et al (2007) Life cycle inventory study on magnesium alloy substitution in vehicles. *Energy* 32:1352–1360. <https://doi.org/10.1016/j.energy.2006.10.020>

4. Mayyas AT, Qattawi A, Mayyas AR, Omar MA (2012) Life cycle assessment-based selection for a sustainable lightweight body-in-white design. *Energy* 39:412–425. <https://doi.org/10.1016/j.energy.2011.12.033>
5. Merklein M, Johannes M, Lechner M, Kuppert A (2014) A review on tailored blanks - Production, applications and evaluation. *J Mater Process Technol* 214:151–164. <https://doi.org/10.1016/j.jmatprotec.2013.08.015>
6. Zadpoor AA, Sinke J, Benedictus R (2007) Mechanics of Tailor Welded Blanks: An Overview. *Key Eng Mater* 344:373–382. <https://doi.org/10.4028/www.scientific.net/kem.344.373>
7. Hong KM, Shin YC (2017) Prospects of laser welding technology in the automotive industry: A review. *J Mater Process Technol* 245:46–69. <https://doi.org/10.1016/j.jmatprotec.2017.02.008>
8. Yan J, Takayama N (2020) Laser-material interactions. *Micro Nanoscale Laser Process Hard Brittle Mater* 37–52. <https://doi.org/10.1016/b978-0-12-816709-0.00003-3>
9. Casalino G, Mortello M, Peyre P (2016) FEM Analysis of Fiber Laser Welding of Titanium and Aluminum. *Procedia CIRP* 41:992–997. <https://doi.org/10.1016/j.procir.2016.01.030>
10. Aghaee Attar M, Ghoreishi M, Malekshahi Beiranvand Z (2020) Prediction of weld geometry, temperature contour and strain distribution in disk laser welding of dissimilar joining between copper & 304 stainless steel. *Optik (Stuttg)* 219:.. <https://doi.org/10.1016/j.ijleo.2020.165288>
11. Goldak J, Chakravarti A, Bibby M (1984) A new finite element model for welding heat sources. *Metall Trans B* 15:299–305. <https://doi.org/10.1007/BF02667333>
12. Du H, Hu L, Liu J, Hu X (2004) A study on the metal flow in full penetration laser beam welding for titanium alloy. *Comput Mater Sci* 29:419–427. <https://doi.org/10.1016/j.commatsci.2003.11.002>
13. Wu CS, Wang HG, Zhang YM (2006) A New Heat Source Model for Keyhole Plasma Arc Welding in FEM. *Weld J* 284–291

14. Farrokhi F, Endelt B, Kristiansen M (2019) A numerical model for full and partial penetration hybrid laser welding of thick-section steels. *Opt Laser Technol* 111:671–686. <https://doi.org/10.1016/j.optlastec.2018.08.059>
15. Zhan X, Mi G, Zhang Q, et al (2017) The hourglass-like heat source model and its application for laser beam welding of 6 mm thickness 1060 steel. *Int J Adv Manuf Technol* 88:2537–2546. <https://doi.org/10.1007/s00170-016-8797-8>
16. Rong Y, Mi G, Xu J, et al (2018) Laser penetration welding of ship steel EH36: A new heat source and application to predict residual stress considering martensite phase transformation. *Mar Struct* 61:256–267. <https://doi.org/10.1016/j.marstruc.2018.06.003>
17. Koo BS, Thasanaraphan P, Nied HF (2019) Numerical simulation of the formation of hourglass welds during laser welding. *J Mater Process Technol* 263:176–185. <https://doi.org/10.1016/j.jmatprotec.2017.12.015>
18. Li Z, Rostam K, Panjehpour A, et al (2020) Experimental and numerical study of temperature field and molten pool dimensions in dissimilar thickness laser welding of Ti6Al4V alloy. *J Manuf Process* 49:438–446. <https://doi.org/10.1016/j.jmapro.2019.11.024>
19. Wang H, Nakanishi M, Kawahito Y (2017) Effects of welding speed on absorption rate in partial and full penetration welding of stainless steel with high brightness and high power laser. *J Mater Process Technol* 249:193–201. <https://doi.org/10.1016/j.jmatprotec.2017.06.014>
20. Kaars J, Mayr P, Koppe K (2018) Determining material data for welding simulation of presshardened steel. *Metals (Basel)* 8:. <https://doi.org/10.3390/met8100740>
21. Swift-Hook DT, Gick AEF (1973) Penetration Welding With Lasers. *Weld J (Miami, Fla)* 52:
22. Sharma RS, Molian P (2011) Weldability of advanced high strength steels using an Yb: YAG disk laser. *J Mater Process Technol* 211:1888–1897. <https://doi.org/10.1016/j.jmatprotec.2011.06.009>
23. THASANARAPHAN P (2012) A Study on the Welding Characteristics of Tailor Welded Blank Metal Sheets Using GTAW and Laser Welding

24. Artinov A, Bakir N, Bachmann M, et al (2018) Weld pool shape observation in high power laser beam welding. In: *Procedia CIRP*. Elsevier B.V., pp 683–686
25. Artinov A, Bachmann M, Rethmeier M (2018) Equivalent heat source approach in a 3D transient heat transfer simulation of full-penetration high power laser beam welding of thick metal plates. *Int J Heat Mass Transf* 122:1003–1013.
<https://doi.org/10.1016/j.ijheatmasstransfer.2018.02.058>